Chevron-beam-based nonlinearity-tunable elastic metamaterial

Geun Ju Jeon and Joo Hwan Oh ®*

Department of Mechanical Engineering, Ulsan National Institute of Science and Technology,
UNIST-gil 50, Eonyang-eup, Ulju-gun, Ulsan, 44919, Korea

In this work, we proposed a chevron-beam-based nonlinearity-tunable elastic metamaterial capable of tuning the nonlinear parameters. Instead of enhancing or suppressing nonlinear phenomena or slightly tuning nonlinearities, the proposed metamaterial directly tunes its nonlinear parameters, allowing much broader manipulation of nonlinear phenomena. Based on the underlying physics, we discovered that the nonlinear parameters of the chevron-beam-based metamaterial are determined by the initial angle. To identify the change in the nonlinear parameters according to the initial angle, we derived an analytical model of the proposed metamaterial to calculate the nonlinear parameters. Based on the analytical model, the actual chevron-beam-based metamaterial is designed. We show that the proposed metamaterial enables nonlinear parameter control and harmonic tuning by numerical methods.

I. INTRODUCTION

Material properties are one of the most significant factors dominating wave propagation. However, the material properties of conventional materials span only a specific and limited range. Due to this issue, previous wave techniques have suffered from various limitations, providing huge technical barriers in engineering applications. Recently, metamaterials allowing abnormal or extreme material properties by artificial unit cell have attracted much attention since they can break through the limitations. For representative instances, metamaterials with negative effective properties including negative density [1–9], negative stiffness [2–10], and negative Poisson's ratio [10–13] have been successfully presented. These abnormal or extreme properties of metamaterials have enabled various new wave physics, such as band gap that prevents wave propagation [14,15], negative refraction [16–18], and extremely high transmission [19–20].

As metamaterials have provided various breakthroughs in linear wave systems, there have been several recent attempts to apply metamaterials in nonlinear systems. For instance, metamaterials that enable amplification of nonlinear phenomena by extreme effective properties [21], and band gap tuning by amplitude-dependent characteristics of nonlinear phenomena [22–24] were studied. Despite previous attempts, however, there is still a limitation that metamaterials' performance is based on given nonlinear parameters. There have been several frontier studies to tune nonlinear parameters by imposing prestress [25–27], but the tuning was achieved by biasing the given nonlinear curve, not by tuning the curve directly. Thus, if metamaterial is based on second order nonlinearity, previous studies may enhance or suppress the related nonlinear effects, but they cannot do anything with the third

nonlinear effects, such as the generation of third harmonic waves. If tailoring nonlinear material properties is enabled with metamaterial, a new field in nonlinear wave physics will be opened allowing various advances in nonlinear wave applications.

In this paper, we propose a nonlinear elastic metamaterial which can directly control the nonlinear parameters. To control the nonlinear parameter, the chevron-beam-based unit cell is introduced. A chevron beam is a structure in which two beams are inclined with constant angle as shown in Fig. 1. In fact, there are several studies which utilized chevron beams due to their capability of buckling [28–30]. However, in this study, we focused on the other characteristic besides buckling; we utilized the unique characteristic of nonreciprocity. When force is exerted along the direction parallel to the symmetric axis, the amount of deformations is different for compression or elongation cases. Here, as a main factor to provide nonlinearity, we used chevron beam's unique characteristic that the deformation mode changes between longitudinal and bending deformation according to the initial angle, the angle between the inclined beam and the axis perpendicular to the symmetric line. When a force parallel to the axis of symmetry is applied to center of the chevron beam, the involved deformation modes under the exerted force change for different initial angles. For instance, if the initial angle is 0 degrees, the inclined beams exhibit bending motions, but if the initial angle is 90 degrees, they will mainly show longitudinal motions. Thus, the resulting deformation becomes different for various initial angles. As a result, the effect of the initial angle, combined with the nonlinearity due to the angle change during deformation, provides tunability of the force-displacement profile, one of the most important nonlinear properties. Therefore, if the relationship between the nonlinear parameter and the initial angle can be figured out, tuning of the nonlinear parameter becomes possible.
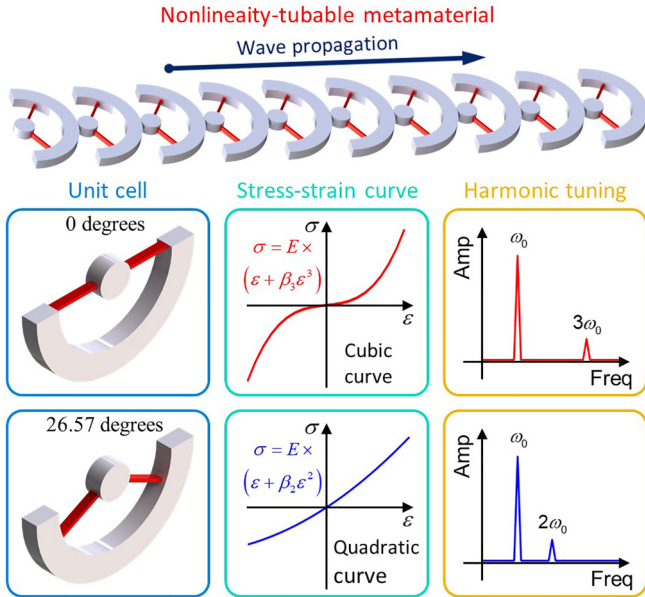
*Corresponding author: joohwan.oh@unist.ac.kr

FIG. 1. Overview of the nonlinearity-tunable elastic metamaterial.

FIG. 2. Equivalent mass-spring system of chevron beam for (a) initial state, (b) equilibrium state.

As a first part of the paper, we theoretically studied the relationship between the nonlinear parameter and the initial angle of the chevron beam. To this end, we considered an equivalent mass-spring system of the chevron beam and derived the nonlinear force-displacement relationship with consideration of the angle change. From the derived force-displacement relation, the nonlinear parameter according to the initial angle is analyzed. After that, the theoretical approach is expanded to take the continuum nature into the consideration. By applying the Euler-Bernoulli beam theory to the chevron beam, the spring coefficients in the equivalent mass-spring system are analytically calculated so that the continuum effect is considered. Surprisingly, not only the nonlinear parameters but also the nonlinear order of the force-displacement relation are tunable with the initial angle, as shown in Fig. 1. Such high tunability has never been studied or reported previously.

Based on the theoretical investigations, we designed an actual nonlinearity-tunable metamaterial that can control the nonlinear parameters by the initial angle, as shown in Fig. 1. The accuracy of the analytical model and the performance of the nonlinearity-tunable metamaterial are validated by numerical methods. In addition, as application and validation of nonlinearity-tunable metamaterial, the well-known harmonic generation is considered. The harmonic generation, one of the most widely applied nonlinear phenomena in practical applications such as nonlinear nondestructive evaluation (NDE), means waves having doubled or tripled frequencies are formed according to the nonlinear parameters. We demonstrate sophisticated harmonic tuning that can dominantly generate the harmonics of the desired order, as shown in Fig. 1. Considering that subharmonic or harmonic wave generation is one of the most frequently used application of nonlinear wave, the nonlinearity tailoring of the proposed metamaterial clearly show the broad possibility of the current research.

The remainder of this paper is organized as follows. First, the background theory of nonlinearity-tunable metamaterial
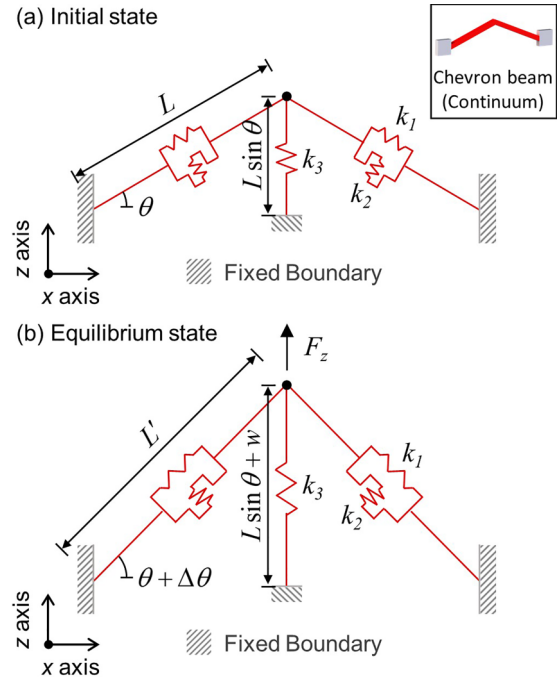
is introduced. In the background theory, the analytical models for nonlinear parameter calculation and harmonics tuning are derived. Second, derived analytical models are numerically validated using the ideal nonlinearity-tunable metamaterial. Third, the feasible nonlinearity-tunable metamaterial capable of nonlinear parameter control and harmonic tuning with a single structure is introduced. Herein, the nonlinearity-tunable metamaterial's design method, band structure, nonlinear parameter control, and harmonic tuning are included. Finally, the conclusions are presented.

II. BACKGROUND THEORY

A. Analytical model for nonlinear parameter calculation

1. Analytical model based on equivalent mass-spring system

As a first step to the nonlinear parameter tuning, theoretical investigations to calculate the nonlinear parameters of a chevron beam are carried out with the equivalent mass-spring system shown in Fig. 2. Figure 2(a) shows the initial state where the beams are aligned along the initial angle, while Fig. 2(b) shows the equilibrium state after the force is applied. In the equivalent mass-spring system, one may wonder why two types of springs, the obliqued springs k_1, k_2, and the vertical spring k_3, are considered. To understand why the two types are considered, it should be remembered that the inclined beams in the chevron beam have two major deformation modes, the longitudinal and bending modes (Note that the shear deformation mode is ignored since the beams are very thin so that the shear deformation mode is negligible compared to other modes). As the angle of the inclined beams changes due to the deformation, the longitudinal mode is significantly altered since the direction of force and deformation change. Thus, the longitudinal modes are expressed by the

obliqued springs which are also largely affected by the angle change. On the other hand, the bending mode is not highly affected by the angle change since the force and deformation directions are unaltered during deformation. Thus, the bending mode has both nonlinear and linear terms, and should be expressed by both the obliqued and vertical springs. As a result, the obliqued springs k_1 are introduced to consider the longitudinal modes, while the obliqued springs k_2 and the vertical spring k_3 are introduced to consider the nonlinear and linear effect of the bending modes, respectively.

From Fig. 2, the force equilibrium equation is derived. Since our goal is to analytically calculate the force-displacement relationship of the chevron beam, the density of the beams is ignored so that the inertia terms are set to be zero. With the assumption, the force equilibrium equation at the tip of the spring is desired as below.

$$F_z = 2[k_1(L' - L)\sin(\theta + \Delta\theta) + k_2(L' - L)\cos(\theta + \Delta\theta)] + k_3 w. \tag{1}$$

In Eq. (1), θ, $\Delta\theta$, L, L', w, and F_z denote initial angle, change in initial angle, initial length of the beam, length of the beam in equilibrium state, z-directional displacement, and z-directional force, respectively. With Pythagorean theorem, L' can be expressed in terms of θ, L, and w as

$$L' = \sqrt{(L\cos\theta)^2 + (L\sin\theta + w)^2}. \tag{2}$$

Accordingly, $\sin(\theta + \Delta\theta)$ and $\cos(\theta + \Delta\theta)$ can be expressed as

$$\sin(\theta + \Delta\theta) = \frac{L\sin\theta + w}{\sqrt{(L\cos\theta)^2 + (L\sin\theta + w)^2}}, \tag{3}$$

$$\cos(\theta + \Delta\theta) = \frac{L\cos\theta}{\sqrt{(L\cos\theta)^2 + (L\sin\theta + w)^2}}. \tag{4}$$

Substituting Eqs. (2)–(4) into Eq. (1), Eq. (1) can be rewritten as

$$F_z = 2\left[k_1 \frac{L\sin\theta + w}{\sqrt{(L\cos\theta)^2 + (L\sin\theta + w)^2}} \right.$$
$$\left. + k_2 \frac{L\cos\theta}{\sqrt{(L\cos\theta)^2 + (L\sin\theta + w)^2}}\right]$$
$$\times [\sqrt{(L\cos\theta)^2 + (L\sin\theta + w)^2} - L] + k_3 w. \tag{5}$$

However, Eq. (5) is too complicated to derive the exact solution. Thus, it is more convenient to express the nonlinear equation as a series of various orders by Taylor expansion as

$$F_z = 0 + [(2\sin^2\theta)k_1 + (2\cos\theta\sin\theta)k_2 + k_3] \times w$$
$$+ \frac{1}{2!}\left[\left\{\frac{6\sin\theta(1 - \sin^2\theta)}{L}\right\}k_1 \right.$$
$$\left. + \left\{\frac{2\cos\theta(1 - 3\sin^2\theta)}{L}\right\}k_2\right] \times w^2$$

$$+ \frac{1}{3!}\left[\left\{\frac{6(1 - 5\sin^2\theta)(1 - \sin^2\theta)}{L^2}\right\}k_1 \right.$$
$$\left. + \left\{\frac{6\cos\theta\sin\theta(5\sin^2\theta - 3)}{L^2}\right\}k_2\right] \times w^3 + \cdots. \tag{6}$$

In this work, we are not focusing on highly nonlinear systems such as the granular crystals, the higher-order terms (higher than w^3) can be ignored. Also, it is much more preferred to express the nonlinearity in the form of stress-strain relation rather than force-displacement relation. From the one-dimensional elasticity, the following equations can be applied:

$$F_z = A_0\sigma, \tag{7a}$$

$$w = L_0\varepsilon. \tag{7b}$$

In Eq. (7), A_0, σ, L_0, and ε denote area where the force is applied, stress, z-directional initial length of the structure, and strain, respectively. Substituting Eqs. (7a) and (7b) into Eq. (6) yields the following stress-strain relation as

$$\sigma = \frac{1}{A_0}L_0[(2\sin^2\theta)k_1 + (2\cos\theta\sin\theta)k_2 + k_3] \times \varepsilon$$
$$+ \frac{1}{A_0}\frac{L_0^2}{L}[3\sin\theta(1 - \sin^2\theta)k_1$$
$$+ \cos\theta(1 - 3\sin^2\theta)k_2] \times \varepsilon^2$$
$$+ \frac{1}{A_0}\frac{L_0^3}{L^2}[(1 - 5\sin^2\theta)(1 - \sin^2\theta)k_1$$
$$+ \cos\theta\sin\theta(5\sin^2\theta - 3)k_2] \times \varepsilon^3 + \cdots. \tag{8}$$

From Eq. (8), it can be found that the spring coefficient k_3 only appears in ε term, the linear term. This is obvious since the spring k_3 is vertically installed so that is unaffected by the angle change during deformation, as explained earlier. Also, Eq. (8) shows that the coefficient of each order is not same, for instance, the ε^2 and ε^3 terms are not same as each other. Thus, it is possible to tailor the system's nonlinearity by adjusting the initial angle of θ, indicating that the desired tunability of nonlinear parameter is indeed possible.

2. Euler-Bernoulli beam theory for chevron beam

Although the equivalent spring system in Fig. 2 clearly showed the possibility of the nonlinear parameter tuning, it cannot be extended to actual metamaterial design unless the relationship between the actual design and the spring coefficients k_1, k_2, and k_3 is revealed. To this end, the half span of a typical chevron beam is considered with the reaction forces, as shown in Fig. 3. Using geometric symmetry, force and moment equilibrium equations can be expressed as

$$\sum F_x = R_{0x} - R_L\cos\theta + \frac{F}{2}\sin\theta = 0, \tag{9a}$$

$$\sum F_z = -R_{0z} + R_L\sin\theta + \frac{F}{2}\cos\theta = 0, \tag{9b}$$

$$\sum M = M_0 - M_L + R_{0x}w(L) + R_{0z}L = 0, \tag{9c}$$

where F is the vertical load applied to the chevron beam, R_{0x} and R_{0z} are the reaction forces acting at the anchor of the
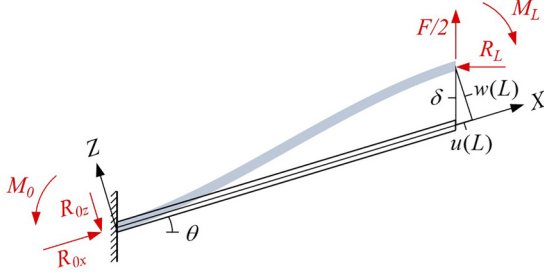
FIG. 3. Continuum structure of chevron beam.

chevron beam, R_L is the reaction force replacing the action of the missing half, M_0 is the moment at the anchor of the chevron beam, and M_L is the moment at the center of the chevron beam. Eq. (9) can be rewritten as follows:

$$R_{0x} = R_L \cos\theta - \frac{F}{2}\sin\theta, \qquad (10a)$$

$$R_{0z} = R_L \sin\theta + \frac{F}{2}\cos\theta, \qquad (10b)$$

$$M_0 = M_L - R_{0x}w(L) - R_{0z}L. \qquad (10c)$$

Applying beam-column theory [31], differential equations for $u(x)$ and $w(x)$ can be expressed as

$$EA\frac{\partial u}{\partial x} = -R_{0x}, \qquad (11)$$

$$EI\frac{\partial^2 w}{\partial x^2} = -R_{0x}w - R_{0z}x - M_0, \qquad (12)$$

where E, A, and I denote Young's modulus, cross-sectional area, and area moment of inertia, respectively. Equations (11) and (12) require five boundary conditions because Eqs. (11) and (12) are first- and second-order differential equations, respectively, and R_{0x} and M_0 are unknowns. Another unknown, R_{0z}, can be solved by Eqs. (10a) and (10b). Five boundary conditions for the chevron beam shown in Fig. 3 are as follows:

$$w(0) = 0, \qquad (13a)$$

$$\frac{\partial w(0)}{\partial x} = 0, \qquad (13b)$$

$$\frac{\partial w(L)}{\partial x} = 0, \qquad (13c)$$

$$u(0) = 0, \qquad (13d)$$

$$u(L) = w(L)\tan\theta. \qquad (13e)$$

Using the boundary conditions, Eqs. (10)–(12) are rearranged as the following two equations (please see the detailed process in Appendix A):

$$w(x) = \left[\tan\theta + \frac{F}{2R_{0x}\cos\theta}\right]\left[\frac{\sin\left(\sqrt{\frac{R_{0x}}{EI}}x\right)}{\sqrt{\frac{EI}{R_{0x}}}}\right.$$

$$\left.+ \frac{\left[\cos\left(\sqrt{\frac{R_{0x}}{EI}}L\right) - 1\right]\left[\cos\left(\sqrt{\frac{R_{0x}}{EI}}x\right) - 1\right]}{\sqrt{\frac{R_{0x}}{EI}}\sin\left(\sqrt{\frac{R_{0x}}{EI}}L\right)} - x\right], \qquad (14)$$

$$\frac{\frac{1}{\tan\theta}\frac{R_{0x}^2 L}{EA}\sqrt{\frac{R_{0x}}{EI}}\sin\left(\sqrt{\frac{R_{0x}}{EI}}L\right)}{L\sqrt{\frac{R_{0x}}{EI}}\sin\left(\sqrt{\frac{R_{0x}}{EI}}L\right) + 2\left[\cos\left(\sqrt{\frac{R_{0x}}{EI}}L\right) - 1\right]}$$

$$= R_{0x}\tan\theta + \frac{F}{2\cos\theta}. \qquad (15)$$

Equation (14) is the force-displacement relation of the chevron beam. The right-hand side terms of Eq. (14) are constants, except for F, θ, and R_{0x}. Since F and θ are input values, if R_{0x} can be expressed by F and θ, the force-displacement relation of the chevron beam can be solved. In fact, by using Eq. (15), reaction force R_{0x} can be calculated with F and θ. However, Eq. (15) is too complicated to be analytically solved, so Eq. (15) is programmed in MATLAB and numerically solved for various input values of initial angle θ and vertical load F. After that, by substituting the numerically calculated reaction force R_{0x} into Eq. (14), the force-displacement relation of the chevron beam is solved.

Based on the Eqs. (14) and (15), the spring coefficients k_1, k_2, and k_3 of actual metamaterial are calculated as follows. First, for various values of θ, Eqs. (14) and (15) are calculated to achieve the force-displacement relationship for various θ. Accordingly, by using the well-known curve-fitting, the plot of Young's modulus versus the initial angle θ is achievable, which is obviously same as the linear term in Eq. (8). Thus, by substituting values of this plot into linear term in Eq. (8), spring coefficients k_1, k_2, and k_3 in Eq. (8) can be calculated. In the linear term of Eq. (8), the only unknowns are spring coefficients k_1, k_2, and k_3, so the spring coefficients can be calculated by Young's modulus for three angles of the plot.

It should be noted that, in Eqs. (14) and (15), the nonlinear effect due to the angle change is not considered, because it has been already considered in the mass-spring system in Eq. (8). Of course, calculating the spring coefficients with nonlinear effect would provide a much accurate result. However, it is extremely complicated to consider the nonlinear effect with the continuum structure because the direction of axial loading and the point where moment is induced change as the angle changes. Moreover, in the current metamaterial, we are focusing on the small nonlinearity case where both the angle change and deformation are not very large. In such a case, it was shown that the change of initial angle does not significantly alter the spring coefficients so that the current Euler-Bernoulli beam approach is still valid [32].

B. Harmonic tuning

From the previous investigations, we showed that the chevron-beam-based metamaterial can tune the nonlinear parameters. However, in the viewpoint of the numerical validation, nonlinear parameters are hard to be accurately evaluated from wave simulations. Therefore, the harmonic generation, one of the most well-known nonlinear phenomena, is considered as a validation of the proposed nonlinear parameter tuning. Especially, we focused on the wave propagation in a nonlinear medium with second- and third-order nonlinearities because the effect of higher-order nonlinearities is generally weak enough to be neglected. The wave equation for a nonlinear medium with second- and third-order nonlin-

earities is as follows [33]:

$$\rho \frac{\partial^2 u}{\partial t^2} - E \frac{\partial^2 u}{\partial x^2} = \beta_2 E \left(\frac{\partial u}{\partial x} \right) \left(\frac{\partial^2 u}{\partial x^2} \right) + \beta_3 E \left(\frac{\partial u}{\partial x} \right)^2 \left(\frac{\partial^2 u}{\partial x^2} \right).$$
(16)

In Eq. (16), ρ, E, u, β_2, and β_3 denote the density, Young's modulus, displacement, second-order nonlinear parameter, and third-order nonlinear parameter, respectively. To obtain the solution, we assume that the fundamental wave of frequency ω and amplitude U_0 is incident from $x = 0$. This boundary condition can be written as follows:

$$u(0, t) = U_0 \cos(\omega t).$$
(17)

By using the perturbation method and the above boundary condition, Eq. (16) can be solved as follows [33]:

$$u(x, t) = U_0 \cos(kx - \omega t) + \frac{\beta_2 U_0^2 \rho \omega^2}{8E} x \cos 2(kx - \omega t)$$

$$- \frac{\beta_3 U_0^3 \rho^{\frac{3}{2}} \omega^3}{8E^{\frac{3}{2}}} x \sin(kx - \omega t)$$

$$+ \frac{\beta_3 U_0^3 \rho^{\frac{3}{2}} \omega^3}{24E^{\frac{3}{2}}} x \sin 3(kx - \omega t).$$
(18)

Equation (18) shows that frequency components corresponding to two and three times of the fundamental frequency ω are generated when a wave propagates in a nonlinear medium with second- and third-order nonlinearities. Since the generated waves are clearly distinguishable because their frequencies are different, the amount of the harmonic generation is well evaluated from wave simulation so that it can be used to validate whether the nonlinear parameters are well-tuned.

As shown in Eq. (8), the metamaterial has various nonlinear terms so that various harmonic waves are generated. In the nonlinear medium, nonlinear phenomena occur continuously as waves propagate. Therefore, once the harmonic waves are generated, the nonlinear interactions between the existing harmonic waves and incident wave take place, generating extra harmonic waves. Among these extra harmonic waves, since the amplitude becomes smaller as the nonlinear order gets higher, we will mainly focus on the extra harmonic

generation due to the frequency conversion between incident wave and second harmonic wave, which have the largest amplitudes. From the frequency conversion, waves having frequency corresponding to the sum and difference of two existing frequencies are newly generated. Focusing on the frequency conversion between incident wave and second harmonic wave whose frequencies are ω and 2ω, the frequency converted waves are summarized as (please see the detailed process in Appendix B).

Frequency-up conversion (3ω):

$$u_{\text{up}}(x, t) = -\frac{\beta_2 \rho}{4E} (U_0) \left(\frac{\beta_2 U_0^2 \rho \omega^2}{8E} \right) (\omega)(2\omega) \frac{x^2}{2}$$

$$\times \cos 3(kx - \omega t).$$
(19)

Frequency-down conversion (ω):

$$u_{\text{down}}(x, t) = -\frac{\beta_2 \rho}{4E} (U_0) \left(\frac{\beta_2 U_0^2 \rho \omega^2}{8E} \right) (\omega)(2\omega) \frac{x^2}{2}$$

$$\times \cos(kx - \omega t).$$
(20)

As a result, substituting Eqs. (19) and (20) into Eq. (18) yields the analytic equation for waves propagating inside a nonlinear media as

$$u(x, t) = U_0 \cos(kx - \omega t) + \frac{\beta_2 U_0^2 \rho \omega^2}{8E} x \cos 2(kx - \omega t)$$

$$- \frac{\beta_3 U_0^3 \rho^{\frac{3}{2}} \omega^3}{8E^{\frac{3}{2}}} x \sin(kx - \omega t)$$

$$+ \frac{\beta_3 U_0^3 \rho^{\frac{3}{2}} \omega^3}{24E^{\frac{3}{2}}} x \sin 3(kx - \omega t)$$

$$- \frac{\beta_2 \rho}{4E} (U_0) \left(\frac{\beta_2 U_0^2 \rho \omega^2}{8E} \right) (\omega)(2\omega) \frac{x^2}{2} \cos(kx - \omega t)$$

$$- \frac{\beta_2 \rho}{4E} (U_0) \left(\frac{\beta_2 U_0^2 \rho \omega^2}{8E} \right) (\omega)(2\omega) \frac{x^2}{2} \cos 3(kx - \omega t).$$
(21)

From Eq. (21), the amplitudes for various frequency components can be obtained as follows.

Fundamental wave (ω):

$$U_\omega = \sqrt{\left[U_0 - \frac{\beta_2 \rho}{4E} (U_0) \left(\frac{\beta_2 U_0^2 \rho \omega^2}{8E} \right) (\omega)(2\omega) \frac{x^2}{2} \right]^2 + \left[\frac{\beta_3 U_0^3 \rho^{\frac{3}{2}} \omega^3}{8E^{\frac{3}{2}}} x \right]^2}.$$
(22)

Second harmonic (2ω):

$$U_{2\omega} = \frac{\beta_2 U_0^2 \rho \omega^2}{8E} x.$$
(23)

Third harmonic (3ω):

$$U_{3\omega} = \sqrt{\left[\frac{\beta_3 U_0^3 \rho^{\frac{3}{2}} \omega^3}{24E^{\frac{3}{2}}} x \right]^2 + \left[\frac{\beta_2 \rho}{4E} (U_0) \left(\frac{\beta_2 U_0^2 \rho \omega^2}{8E} \right) (\omega)(2\omega) \frac{x^2}{2} \right]^2}.$$
(24)

Finally, the tunability of the metamaterial's nonlinear parameter is validated as follows. First, from the metamaterial design, the equivalent spring coefficients k_1, k_2, and k_3 are

evaluated, as explained in the previous section. After that, the nonlinear parameters are calculated from Eq. (8). Finally, the amplitudes of the harmonic waves are analytically predicted

from Eqs. (22)–(24). After the analytic prediction, the numerical simulation with the same metamaterial design is carried out and the results are compared with the predicted values.

III. IDEAL NONLINEARITY-TUNABLE METAMATERIAL

In this section, the chevron-beam-based metamaterial is actually designed and its tunability performance is validated. In actual metamaterial, there is unavoidable difference from the continuum model used in Euler-Bernoulli beam theory for chevron beam because the fixed and roller boundary conditions cannot be strictly applied. Due to this difference, it is hard to validate the theoretical approach shown in the previous section unless the continuum metamaterial is specially designed. Here, before considering any feasible metamaterial, we will introduce the ideal metamaterial in which various special conditions are introduced to minimize the difference so that the numerical validation is possible.

There are several considerations in the design of the ideal nonlinearity-tunable metamaterial. First, the chevron beams of the ideal nonlinearity-tunable metamaterial should be designed to be as similar to the analytical model as possible. In the analytical model, a fixed boundary condition is applied to the anchor of the chevron beam, and the roller condition is imposed to the other end. However, if the fixed boundary condition is applied to the anchor of the chevron beam in the ideal nonlinearity-tunable metamaterial, waves cannot propagate. Conversely, if no boundary conditions are given, the magnitude of the moment acting at the anchor of the chevron beam deviates from the analytical model, and spring coefficients, $k_1 \sim k_3$, cannot be calculated accurately. Therefore, in the ideal nonlinearity-tunable metamaterial, a specific boundary condition that suppresses any motion in the direction perpendicular to the boundary is applied to the anchor and the other end of the chevron beam so that the beams act almost same as in the theoretical approach. In addition, the geometric variables other than the initial angle should be almost constant for various initial angles. Of course, in the continuum metamaterial, there is unavoidable change of length, height, and other geometric variables if the initial angle changes. Nevertheless, these undesired changes are minimized since we focus on the nonlinear parameter change due to the initial angle change only. As a result, the ideal nonlinearity-tunable metamaterial is designed in Fig. 4. Note that although the chevron beam part is colored in red for convenience, all structure is based on a same material of aluminum, whose material parameters are density $\rho = 2700 \, (\text{kg/m}^3)$, Young's modulus $E = 70 \, (\text{GPa})$, and Poisson's ratio $\upsilon = 0.32$. For all simulation, the commercial program COMSOL is used.

First, to check whether the nonlinear parameters are indeed tunable, the static tensile test is numerically carried out. The tensile test imposes static force and measures the deformation so that the metamaterial's force-displacement relationship is evaluated. The simulation setting is shown in Fig. 5(a). From the evaluated force-displacement relationship, the curve fitting is carried out to measure the Young's modulus E and nonlinear parameters β_2, β_3 for various initial angles. After that, numerically calculated E, β_2, and β_3 are compared with the analytically predicted values (the analytic process to predict the parameters was explained in the previous section).
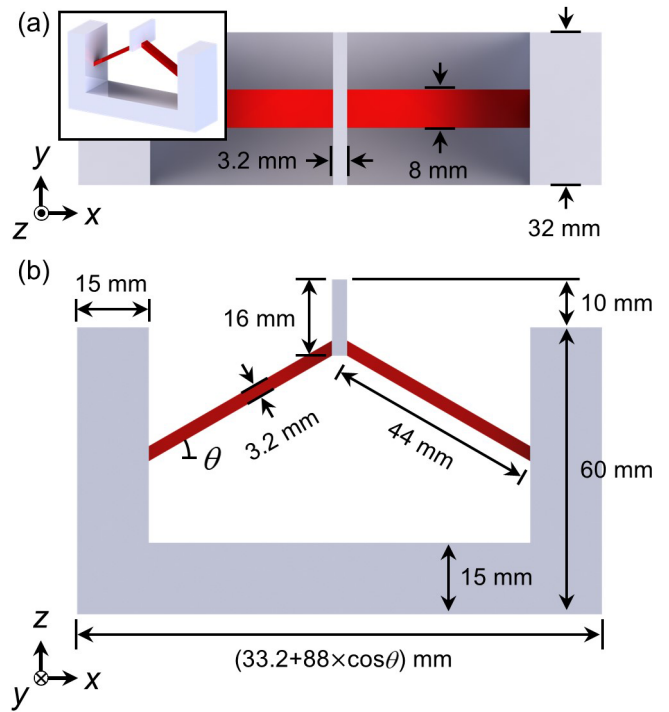

FIG. 4. Detailed geometries and sizes of ideal nonlinearity-tunable metamaterial: (a) top view, (b) front view.

Figures 5(b)–5(d) plot the numerically and analytically calculated parameters. As shown in Fig. 5(b)–5(d), analytical and numerical results show similar trends. Also, from Figs. 5(c) and 5(d), it is clearly shown that the metamaterial's nonlinear parameters are indeed tunable with the initial angle. However, in Figs. 5(b)–5(d), there are non-negligible differ-
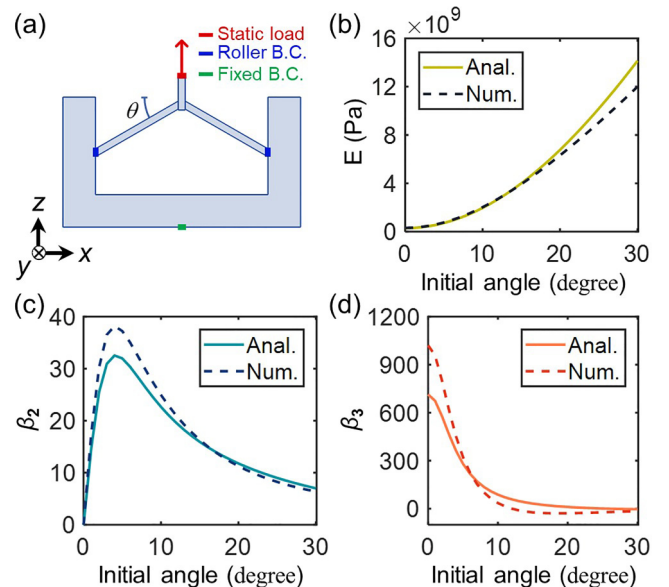

FIG. 5. (a) Numerical simulation settings of tensile test for the ideal nonlinearity-tunable metamaterial. Analytical and numerical results for the (b) Young's modulus, (c) second nonlinear parameter, and (d) third nonlinear parameter, respectively.
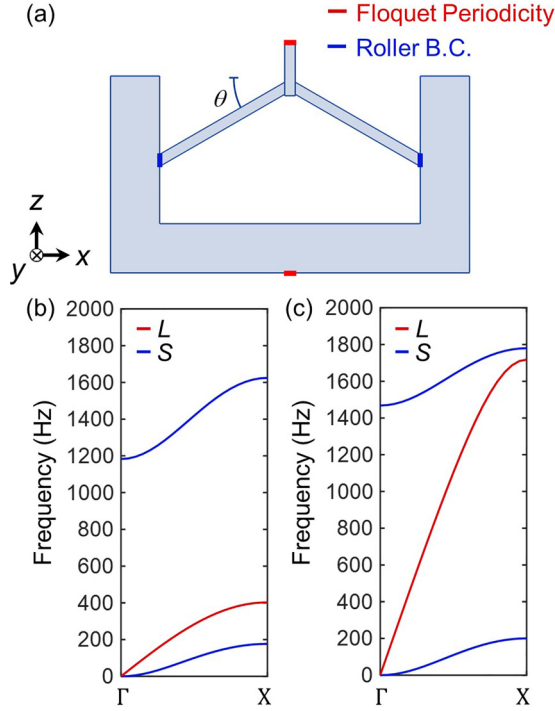
FIG. 6. (a) Numerical simulation settings of the band structure calculation. Band structures of ideal nonlinearity-tunable metamaterial for (b) $\theta = 0$ degrees, (c) $\theta = 30$ degrees. The red and blue lines indicate longitudinal and shear wave modes, respectively.
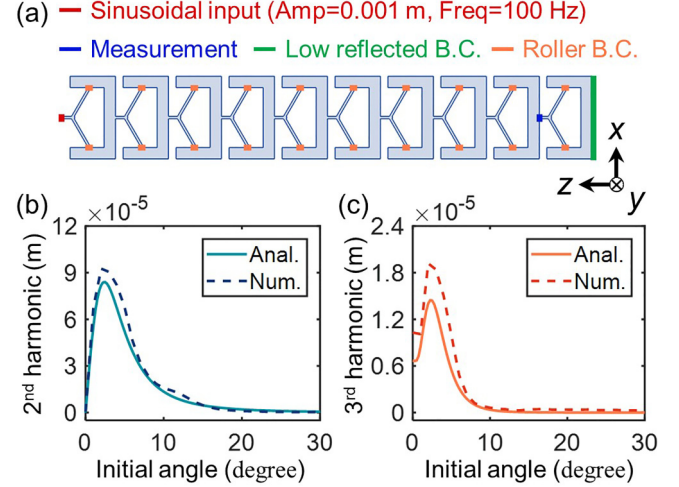

FIG. 7. (a) Numerical simulation settings of transient analysis for the ideal nonlinearity-tunable metamaterial. Analytical and numerical results for the amplitudes of (b) second harmonic and (c) third harmonic, respectively.

ences between the analytic and numerical results due to the deformation of the structure other than the chevron beam. In the analytic model, only the chevron beam is assumed to be deformed. However, in the continuum model, non-negligible deformation occurs at the mass parts because they are not rigid bodies. These inevitable deformations in the continuum models lead to significant differences between analytic and numerical results.

In addition, the nonlinear parameter tuning is checked by the harmonic generation. Before the wave simulation, however, it should be checked whether the metamaterials have band gap for any harmonics. As shown in previous studies [21], metamaterial's band gap suppresses any nonlinear effects including the harmonic generation. Thus, the metamaterial's band gap should be calculated first, and based on the band structure, the wave simulation is carried out with the frequency ω whose second and third harmonics, 2ω and 3ω, do not belong to any band gap frequencies. Figure 6(a) shows the simulation setting to calculate the band structure. Here, we adopted the well-known approach of imposing the Floquet boundary condition and carrying out eigenfrequency analysis for various wave vectors. The Floquet condition is only valid for linear system, but with the small nonlinear system as in the current research, it is still acceptable. For more details about the validation of using the Floquet condition in the nonlinear system, see Appendix C.

Figures 6(b) and 6(c) plot the band structure for the metamaterial with initial angle of $\theta = 0$ degrees and $\theta = 30$ degrees, respectively. As shown in Fig. 5(b), the Young's modulus increases as the initial angle increases. In other

words, the metamaterial with $\theta = 0$ degrees has the lowest band gap frequency. For the metamaterial with $\theta = 0$ degrees, the band gap of longitudinal wave starts from 391.8 Hz. Therefore, we choose the initial actuation frequency to be 100 Hz so that the band gap or slow wave phenomenon around the band gap do not affect the harmonic generation.

Figure 7(a) is the numerical simulation setting to validate the nonlinear tunability of the metamaterial with harmonics. As shown in Fig. 7(a), ten units of the ideal nonlinearity-tunable metamaterial are arranged. At the left end of the metamaterial layer, the longitudinal wave is actuated by imposing the displacement condition as a sine function with the frequency of 100 Hz. Since various frequencies are involved, the transient wave simulation instead of the general time harmonic simulations are carried out. After the simulation, the transmitted wave is measured at the boundary between the ninth unit cell and the tenth unit cell. To suppress any reflected wave, a pseudoperfectly matched layer (pseudo-PML) is imposed to the right end of the ideal nonlinearity-tunable metamaterial. Since the general PML is only available for time harmonic case, it is not suitable for the current time-transient simulation where various frequency components are generated. Thus, we impose the pseudo-PML by attaching the same metamaterials whose properties and shape are same but having damping value that gradually increases so that the waves are dissipated without any reflections. Finally, the measured data is postprocessed by Fourier transformation to clearly see the amplitude of each harmonic waves.

The amplitudes of second and third harmonics, corresponding to 200 and 300 Hz waves, are plotted in Figs. 7(b) and 7(c). Both the numerically and analytically calculated results are plotted; the process to analytically calculate each amplitude is given in the previous section. As shown in Figs. 7(b) and 7(c), the analytic and numerical results show similar trends, clearly showing the harmonic tunability of the ideal nonlinearity-tunable metamaterial. Note that the differences observed in Figs. 7(b) and 7(c) are mainly due to
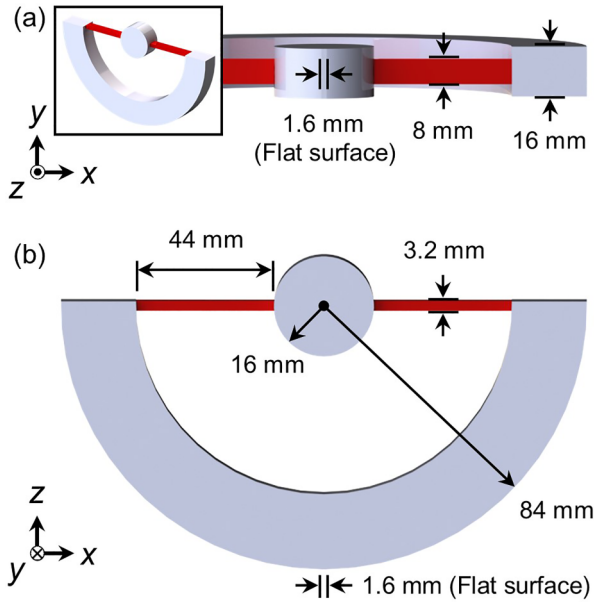
FIG. 8. Detailed geometries and sizes of feasible nonlinearity-tunable metamaterial: (a) top view, (b) front view.
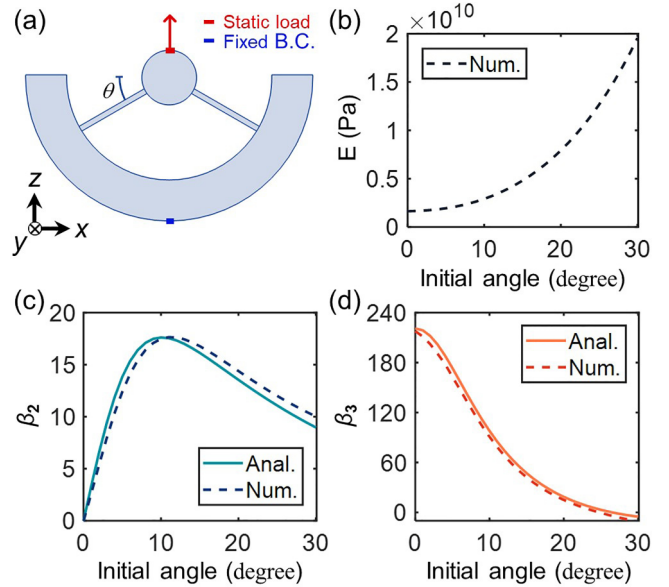

FIG. 9. (a) Numerical simulation settings of tensile test for the feasible nonlinearity-tunable metamaterial. Analytical and numerical results for (b) Young's modulus, (c) second nonlinear parameter, and (d) third nonlinear parameter, respectively.

the limitation of the perturbation method. In the perturbation method, the small nonlinearity assumption is used so that the higher-order perturbation terms are ignored. However, such an assumption inevitably generates errors unless infinite-order perturbations are performed. Since in general only the first-order perturbation is considered, the error inevitably occurs as shown in Fig. 7.

IV. FEASIBLE NONLINEARITY-TUNABLE METAMATERIAL

Although the ideal metamaterial clearly validated the performance of the nonlinear parameter tunability, the boundary conditions are somewhat unrealistic so that it is almost impossible to actually realize it. Thus, we repeat the numerical validation for metamaterial without such boundary conditions to show that our nonlinearity-tunable metamaterial is feasible. Figure 8 shows the feasible nonlinearity-tunable metamaterial. Again, note that the chevron beams are plotted in red color for better illustration, but all metamaterials are made of same material, aluminum.

It is worth emphasizing several design issues of the feasible metamaterial. Unlike in the ideal case where specific condition is applied to the anchor of the chevron beam, feasible metamaterials cannot utilize such an unrealistic method. Therefore, in order to mimic the boundary condition of the analytical model, the chevron beam's stiffness should be designed as soft as possible compared to the other parts so that most of the deformation occurs in the chevron beam. However, if the difference in stiffness is too large, wave speed is too slowed down so that the transient analysis becomes almost impossible. In addition, slow wave speed yields low band gap formation, which makes the harmonic wave simulation extremely hard. Thus, the thickness of the chevron beam in Fig. 8 is properly chosen to avoid the issues related to the slow wave. In addition, the other parts which act as a mass

is designed in an arc form so that its stiffness becomes high without using too heavy mass.

Based on the feasible metamaterial, the nonlinearity tunability is numerically validated. First, as in the ideal case, the tensile test is numerically carried out to check the nonlinear parameters. Figure 9(a) shows the numerical setting of the tensile test. While the numerical process is same as the ideal case, the analytic prediction is different. Since the feasible metamaterial has no specific boundary condition, its stiffness cannot be analytically calculated via the Euler-Bernoulli beam theory because the spring and mass are not clearly distinguishable in the feasible metamaterial and not only the chevron beams but also other parts are involved in the deformation. Thus, from the numerically measured Young's modulus, the spring coefficients k_1, k_2, and k_3 are evaluated by curve fitting. The calculated values are as follows: $k_1 = 7.67 \times 10^6$ N/m, $k_2 = 1.83 \times 10^{-5}$ N/m, and $k_3 = 5.38 \times 10^5$ N/m. After that, the nonlinear parameters β_2 and β_3 are analytically predicted with the evaluated spring coefficients. Figures 9(c) and 9(d) plot the numerically and analytically predicted nonlinear parameters. Again, the numerical results and the analytic results are in good agreement and the nonlinear parameters of the feasible nonlinearity-tunable metamaterial are determined by the initial angle. In other words, it is clearly validated that the feasible nonlinearity-tunable metamaterial can control nonlinear parameters by the initial angle with a single structure. It is worth noting that the nonlinear parameter in aluminum is around 5–10 for unfatigued aluminum and 14–17 for fatigued aluminum [34]. From the difference in the nonlinear parameter between unfatigued and fatigued aluminum, the nonlinear NDE applications check whether the sample is fatigued or not. On the other hand, Figs. 9(c)–9(d) show that the proposed metamaterial has a wide nonlinearity tunable range from 0 to 17.64, which means that the nonlinear parameters achievable
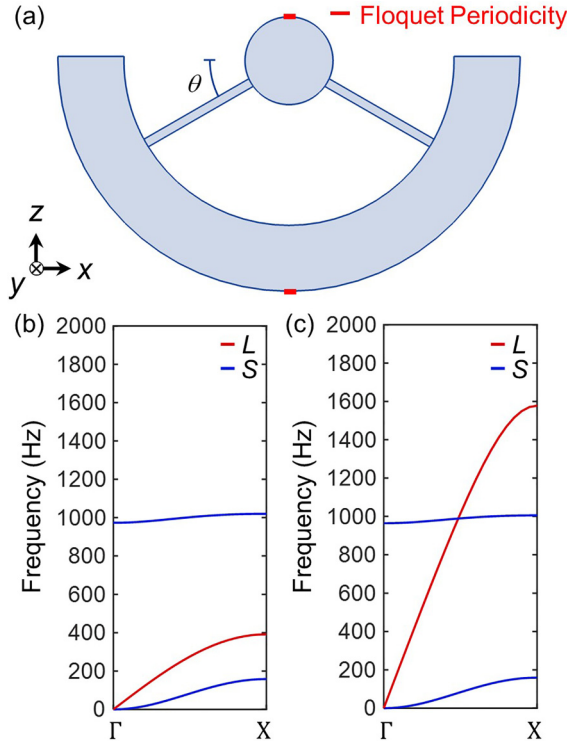
FIG. 10. (a) Numerical simulation settings of the band structure calculation. Band structures of feasible nonlinearity-tunable metamaterial for (b) $\theta = 0$ degrees, (c) $\theta = 30$ degrees. The red and blue lines indicate longitudinal and shear branches, respectively.

with the current metamaterial are sufficiently large and significantly broad in the viewpoint of actual applications.

Finally, the transient analyses are carried out to check the harmonic generation. Before the transient analyses, the band structure of the feasible metamaterial should be calculated to avoid any effect due to the band gap. Figure 10 shows the simulation setting and the band structure at $\theta = 0$ degrees and $\theta = 30$ degrees. From the band structures shown in Figs. 10(b) and 10(c), it was shown that the frequency below 392 Hz is always pass band for any initial angles. Thus, the actuation frequency is chosen as 100 Hz so that second and third harmonics, 200 and 300 Hz, are not affected by the band gap.

Figure 11(a) shows the simulation setting for the harmonic generation. The simulation procedures are all same, except that the incident amplitude is increased to 5 mm to more clearly see nonlinear effects. Figures 11(b) and 11(c) plot the amplitude of the second and third harmonics at the point between ninth and tenth unit cell. As shown in Figs. 11(b) and 11(c), the analytical and numerical results show similar trends, clearly showing the harmonic tunability of the feasible nonlinearity-tunable metamaterial. Note that as in the case shown with Fig. 7, there are inevitable errors between the analytic and numerical results due to the limit of the perturbation method.

Before the conclusion, several meaningful cases of the nonlinearity-tunable metamaterials are explained. First, since k_2 is almost zero value, the nonlinear parameter β_2 becomes almost zero at initial angle of $\theta = 0$ degrees as shown in
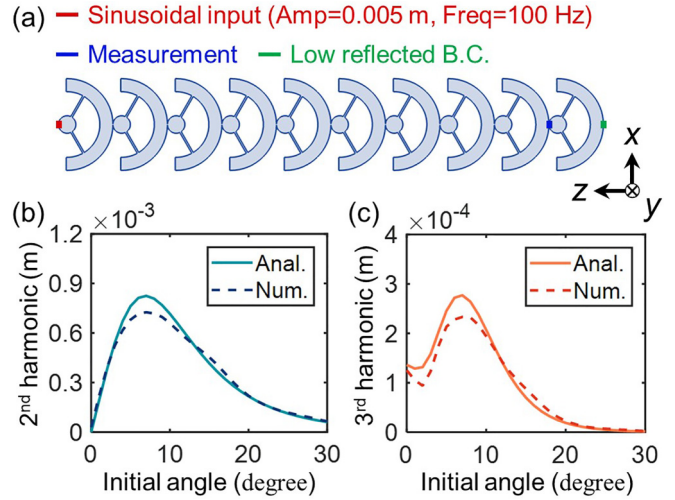

FIG. 11. (a) Numerical simulation settings of transient analysis for the feasible nonlinearity-tunable metamaterial. Analytical and numerical results for the amplitudes of (b) second harmonic and (c) third harmonic, respectively.

Eq. (8). Thus, from the theory, the second harmonic generation of the metamaterial with $\theta = 0$ degrees becomes much smaller than the third harmonic generation. On the other hand, according to the theory, the nonlinear parameter β_3 becomes zero and the third harmonic generation disappears at $\theta = 26.57$ degrees. Furthermore, it is also possible to make the second and third harmonic waves equal at $\theta = 0.5$ degrees, and maximize both harmonic waves at $\theta = 7$ degrees. Figures 12(a)–12(d) show the numerical simulation results of meaningful cases at $\theta = 0$ degrees, $\theta = 26.57$ degrees, $\theta = 0.5$ degrees, and $\theta = 7$ degrees, respectively. As can be seen in Figs. 12(a) and 12(b), the second harmonic becomes ex-
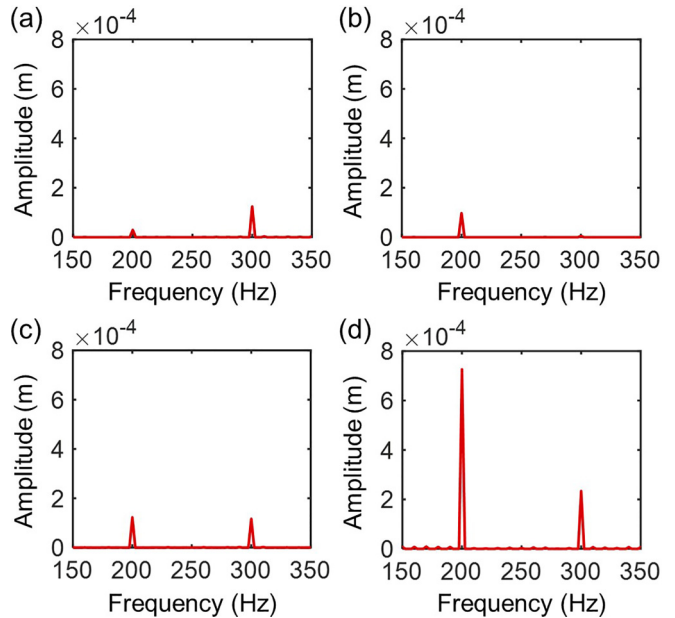

FIG. 12. Frequency domain data for the second and third harmonics with the initial angle of (a) 0 degrees, (b) 26.57 degrees, (c) 0.5 degrees, (d) 7 degrees.

tremely small at $\theta = 0$ degrees, while the third harmonic almost disappears at $\theta = 26.57$ degrees, as predicted from the theory. In addition, Figs. 12(c) and 12(d) show the case when the amplitudes of second and third harmonic waves become equal at $\theta = 0.5$ degrees, and maximized at $\theta = 7$ degrees. These results show that the nonlinearity-tunable metamaterial not only can enhance or weaken nonlinear effects but also can tailor whether the material's nonlinearity is governed by second or third order nonlinearities. With the currently existing nonlinear materials, it is impossible to tailor the material's nonlinear order, indicating that our metamaterial has extremely high tunability and may open a different field to nonlinear-wave-based devices.

V. CONCLUSIONS

In this work, we proposed a chevron-beam-based nonlinearity-tunable metamaterial capable of nonlinear parameter control and harmonic tuning with a single structure. Based on the equivalent mass-spring system and Euler-Bernoulli theory for chevron beam, we derived the analytical model that can calculate nonlinear parameters according to the initial angle. In addition, we investigated nonlinear phenomena affecting the amplitude of harmonics and derived the analytical model for harmonic tuning. The analytical model for nonlinear parameter calculation and harmonic tuning were numerically validated by using an ideal nonlinearity-tunable metamaterial. Based on the analytical models, the feasible nonlinearity-tunable metamaterial was designed. Using the feasible nonlinearity-tunable metamaterial, we successfully demonstrated the nonlinear parameter control and the harmonic tuning.

In the current research, the experimental results were not included due to the issue of plastic deformation and material nonlinearity caused by the machining process. During the machining process, various microcracks are formed inside the metamaterial samples so that undesired plastic deformation or material nonlinearity takes place. However, if any new metamaterial geometry is introduced with the fillets or other well-known stress-relieving structures, we believe that our idea of nonlinearity tunable metamaterial can provide actual tuning of nonlinearity itself. Considering that nonlinear wave phenomena originate from nonlinear parameters, the results presented herein would be useful for sophisticated control of the nonlinear elastic wave phenomena.

ACKNOWLEDGMENTS

APPENDIX A: EULER-BERNIULLI BEAM THEORY FOR CHEVRON BEAM

In Appendix A, the detailed derivation process of the Euler-Bernoulli beam theory for a chevron beam is explained. As mentioned in Sec. II, force and moment equilibrium equations, differential equations, and boundary conditions for a typical chevron beam are as follows.

Force and moment equilibrium equations:

$$R_{0x} = R_L \cos\theta - \frac{F}{2}\sin\theta, \tag{A1}$$

$$R_{0z} = R_L \sin\theta + \frac{F}{2}\cos\theta, \tag{A2}$$

$$M_0 = M_L - R_{0x}w(L) - R_{0z}L. \tag{A3}$$

Differential equations for $u(x)$ and $w(x)$:

$$EA\frac{\partial u}{\partial x} = -R_{0x}, \tag{A4}$$

$$EI\frac{\partial^2 w}{\partial x^2} = -R_{0x}w - R_{0z}x - M_0, \tag{A5}$$

Boundary conditions:

$$w(0) = 0, \tag{A6}$$

$$\frac{\partial w(0)}{\partial x} = 0, \tag{A7}$$

$$\frac{\partial w(L)}{\partial x} = 0, \tag{A8}$$

$$u(0) = 0, \tag{A9}$$

$$u(L) = w(L)\tan\theta. \tag{A10}$$

Integrating Eq. (A1) along L yields

$$u(L) - u(0) = -\frac{R_{0x}L}{EA}. \tag{A11}$$

Substituting Eqs. (A9) and (A10) into Eq. (A11) yields

$$w(L) = -\frac{1}{\tan\theta}\frac{R_{0x}L}{EA}. \tag{A12}$$

Solving the second-order Eq. (A5) yields

$$w(x) = -\frac{R_{0z}}{R_{0x}}x - \frac{M_0}{R_{0x}} + K_1\cos\left(\sqrt{\frac{R_{0x}}{EI}}x\right)$$
$$+ K_2\sin\left(\sqrt{\frac{R_{0x}}{EI}}x\right). \tag{A13}$$

Substituting $x = 0$ and Eq. (A6) into Eq. (A13), coefficient k_1 can be obtained as follows:

$$K_1 = \frac{M_0}{R_{0x}}. \tag{A14}$$

Differentiating Eq. (A13) yields

$$\frac{\partial}{\partial x}[w(x)] = -\frac{R_{0z}}{R_{0x}} - K_1\sqrt{\frac{R_{0x}}{EI}}\sin\left(\sqrt{\frac{R_{0x}}{EI}}x\right)$$
$$+ K_2\sqrt{\frac{R_{0x}}{EI}}\cos\left(\sqrt{\frac{R_{0x}}{EI}}x\right). \tag{A15}$$

Substituting $x = 0$ and Eq. (A7) into Eq. (A15), coefficient K_2 can be obtained as follows:

$$K_2 = \sqrt{\frac{EI}{R_{0x}}}\frac{R_{0z}}{R_{0x}}. \tag{A16}$$

Substituting Eq. (A14) and Eq. (A16) into Eq. (A13) yields

$$w(x) = -\frac{R_{0z}}{R_{0x}}x - \frac{M_0}{R_{0x}} + \frac{M_0}{R_{0x}}\cos\left(\sqrt{\frac{R_{0x}}{EI}}x\right)$$
$$+ \sqrt{\frac{EI}{R_{0x}}}\frac{R_{0z}}{R_{0x}}\sin\left(\sqrt{\frac{R_{0x}}{EI}}x\right). \quad \text{(A17)}$$

Differentiating Eq. (A17) yields

$$\frac{\partial w(x)}{\partial x} = -\frac{R_{0z}}{R_{0x}} - \sqrt{\frac{R_{0x}}{EI}}\frac{M_0}{R_{0x}}\sin\left(\sqrt{\frac{R_{0x}}{EI}}x\right)$$

$$+ \frac{R_{0z}}{R_{0x}}\cos\left(\sqrt{\frac{R_{0x}}{EI}}x\right). \quad \text{(A18)}$$

Substituting $x = L$ and Eq. (A8) into Eq. (A18), yields

$$0 = -\frac{R_{0z}}{R_{0x}} - \sqrt{\frac{R_{0x}}{EI}}\frac{M_0}{R_{0x}}\sin\left(\sqrt{\frac{R_{0x}}{EI}}L\right) + \frac{R_{0z}}{R_{0x}}\cos\left(\sqrt{\frac{R_{0x}}{EI}}L\right). \quad \text{(A19)}$$

Equation (A19) can be rearranged as

$$M_0 = \frac{R_{0z}\left[\cos\left(\sqrt{\frac{R_{0x}}{EI}}L\right) - 1\right]}{\sqrt{\frac{R_{0x}}{EI}}\sin\left(\sqrt{\frac{R_{0x}}{EI}}L\right)}. \quad \text{(A20)}$$

Substituting Eq. (A20) into Eq. (A17), yields

$$w(x) = -\frac{R_{0z}}{R_{0x}}x + \frac{R_{0z}}{R_{0x}}\frac{\left[\cos\left(\sqrt{\frac{R_{0x}}{EI}}L\right) - 1\right]\left[\cos\left(\sqrt{\frac{R_{0x}}{EI}}x\right) - 1\right]}{\sqrt{\frac{R_{0x}}{EI}}\sin\left(\sqrt{\frac{R_{0x}}{EI}}L\right)} + \sqrt{\frac{EI}{R_{0x}}}\frac{R_{0z}}{R_{0x}}\sin\left(\sqrt{\frac{R_{0x}}{EI}}x\right). \quad \text{(A21)}$$

Equation (A21) can be rearranged as

$$w(x) = \frac{R_{0z}}{R_{0x}}\left[\frac{\sin\left(\sqrt{\frac{R_{0x}}{EI}}x\right)}{\sqrt{\frac{EI}{R_{0x}}}} + \frac{\left[\cos\left(\sqrt{\frac{R_{0x}}{EI}}L\right) - 1\right]\left[\cos\left(\sqrt{\frac{R_{0x}}{EI}}x\right) - 1\right]}{\sqrt{\frac{R_{0x}}{EI}}\sin\left(\sqrt{\frac{R_{0x}}{EI}}L\right)} - x\right]. \quad \text{(A22)}$$

From Eqs. (A1) and (A2), relation between R_{0x} and R_{0z} can be obtained as follows:

$$\frac{R_{0z}}{R_{0x}} = \tan\theta + \frac{F}{2R_{0x}\cos\theta}. \quad \text{(A23)}$$

Substituting Eq. (A23) into Eq. (A22), yields

$$w(x) = \left[\tan\theta + \frac{F}{2R_{0x}\cos\theta}\right]\left[\frac{\sin\left(\sqrt{\frac{R_{0x}}{EI}}x\right)}{\sqrt{\frac{EI}{R_{0x}}}} + \frac{\left[\cos\left(\sqrt{\frac{R_{0x}}{EI}}L\right) - 1\right]\left[\cos\left(\sqrt{\frac{R_{0x}}{EI}}x\right) - 1\right]}{\sqrt{\frac{R_{0x}}{EI}}\sin\left(\sqrt{\frac{R_{0x}}{EI}}L\right)} - x\right]. \quad \text{(A24)}$$

Equation (A24) is the force-displacement relation of the chevron beam. The right-hand side terms of Eq. (A24) are constants, except for F, θ, and R_{0x}. Since F and θ are input values, if R_{0x} can be expressed by F and θ, the force-displacement relation of the chevron beam can be solved. Reaction force R_{0x}, corresponding to input values F and θ, can be obtained with the following derivation process.

Substituting $x = L$ and Eq. (A12) into Eq. (A17), yields

$$-\frac{1}{\tan\theta}\frac{R_{0x}L}{EA} = -\frac{R_{0z}}{R_{0x}}L - \frac{M_0}{R_{0x}} + \frac{M_0}{R_{0x}}\cos\left(\sqrt{\frac{R_{0x}}{EI}}L\right)$$
$$+ \sqrt{\frac{EI}{R_{0x}}}\frac{R_{0z}}{R_{0x}}\sin\left(\sqrt{\frac{R_{0x}}{EI}}L\right). \quad \text{(A25)}$$

Equation (A25) can be rearranged as

$$M_0 = \frac{R_{0z}\left[L - \sqrt{\frac{EI}{R_{0x}}}\sin\left(\sqrt{\frac{R_{0x}}{EI}}L\right)\right] - \frac{1}{\tan\theta}\frac{R_{0x}^2 L}{EA}}{\cos\left(\sqrt{\frac{R_{0x}}{EI}}L\right) - 1}. \quad \text{(A26)}$$

Subtracting Eq. (A26) from Eq. (A20) yields

$$\frac{R_{0z}\left[L - \sqrt{\frac{EI}{R_{0x}}}\sin\left(\sqrt{\frac{R_{0x}}{EI}}L\right)\right] - \frac{1}{\tan\theta}\frac{R_{0x}^2 L}{EA}}{\cos\left(\sqrt{\frac{R_{0x}}{EI}}L\right) - 1}$$
$$= \frac{R_{0z}\left[\cos\left(\sqrt{\frac{R_{0x}}{EI}}L\right) - 1\right]}{\sqrt{\frac{R_{0x}}{EI}}\sin\left(\sqrt{\frac{R_{0x}}{EI}}L\right)}. \quad \text{(A27)}$$

Equation (A27) can be rearranged as

$$R_{0z} = \frac{\frac{1}{\tan\theta}\frac{R_{0x}^2 L}{EA}\sqrt{\frac{R_{0x}}{EI}}\sin\left(\sqrt{\frac{R_{0x}}{EI}}L\right)}{L\sqrt{\frac{R_{0x}}{EI}}\sin\left(\sqrt{\frac{R_{0x}}{EI}}L\right) + 2\left[\cos\left(\sqrt{\frac{R_{0x}}{EI}}L\right) - 1\right]}. \quad \text{(A28)}$$

Substituting Eq. (A28) into Eq. (A2) yields

$$\frac{\frac{1}{\tan\theta}\frac{R_{0x}^2 L}{EA}\sqrt{\frac{R_{0x}}{EI}}\sin\left(\sqrt{\frac{R_{0x}}{EI}}L\right)}{L\sqrt{\frac{R_{0x}}{EI}}\sin\left(\sqrt{\frac{R_{0x}}{EI}}L\right) + 2\left[\cos\left(\sqrt{\frac{R_{0x}}{EI}}L\right) - 1\right]}$$
$$= R_L\sin\theta + \frac{F}{2}\cos\theta. \quad \text{(A29)}$$

Equation (A1) can be rearranged as

$$R_L = \frac{R_{0x}}{\cos\theta} + \frac{F}{2}\tan\theta. \tag{A30}$$

Substituting Eq. (A30) into Eq. (A29) yields

$$\frac{\frac{1}{\tan\theta}\frac{R_{0x}^2 L}{EA}\sqrt{\frac{R_{0x}}{EI}}\sin\left(\sqrt{\frac{R_{0x}}{EI}}L\right)}{L\sqrt{\frac{R_{0x}}{EI}}\sin\left(\sqrt{\frac{R_{0x}}{EI}}L\right) + 2\left[\cos\left(\sqrt{\frac{R_{0x}}{EI}}L\right) - 1\right]}$$

$$= R_{0x}\tan\theta + \frac{F}{2\cos\theta}. \tag{A31}$$

Using Eq. (A31), reaction force R_{0x}, corresponding to input values F and θ, can be calculated.

APPENDIX B: SECONDARY NONLINEAR PHENOMENA

To consider the secondary nonlinear phenomena, we assume that the fundamental wave and the nonlinear frequency component propagate simultaneously in the nonlinear medium. Here, as a nonlinear frequency component, a second harmonic is considered, whose amplitude is large enough to cause secondary nonlinear phenomena. Also, secondary nonlinear phenomena generated by third-order nonlinearity are very small compared to second-order nonlinearity so the wave equation including only the second-order nonlinearity is considered for secondary nonlinear phenomena. The second-order nonlinear wave equation is as follows:

$$\rho\frac{\partial^2 u}{\partial t^2} - E\frac{\partial^2 u}{\partial x^2} = \beta_2 E\left(\frac{\partial u}{\partial x}\right)\left(\frac{\partial^2 u}{\partial x^2}\right). \tag{B1}$$

In Eq. (B1), ρ, E, u, and β_2 denote the density, Young's modulus, displacement, and second-order nonlinear parameter, respectively. Next, we derive the solution for secondary nonlinear phenomena. To obtain the solution for secondary nonlinear phenomena, we assume that the fundamental wave of frequency ω and amplitude U_0 and second harmonic of frequency 2ω and amplitude U_1 are actuated from $x = 0$. This can be written as the boundary condition as follows:

$$u(0, t) = U_0 \cos(-\omega t) + U_1 \cos(-2\omega t). \tag{B2}$$

With this boundary condition, derived solution for Eq. (B1) by perturbation method is as follows [21]:

$$u(x, t) = U_0 \cos(kx - \omega t) + U_1 \cos 2(kx - \omega t)$$

$$+ \frac{\beta_2 U_0^2 \rho\omega^2}{8E}x\cos 2(kx - \omega t)$$

$$+ \frac{\beta_2 U_1^2 \rho(2\omega)^2}{8E}x\cos 4(kx - \omega t)$$

$$- \frac{\beta_2 U_0 U_1 \rho(\omega)(2\omega)}{4E}x\cos 3(kx - \omega t)$$

$$- \frac{\beta_2 U_0 U_1 \rho(\omega)(2\omega)}{4E}x\cos(kx - \omega t). \tag{B3}$$

Since the entire equation is complex, we classified the amplitude of each term according to frequency, except the fundamental wave.

Second harmonic 1 (2ω):

$$U_{h1} = \frac{\beta_2 U_0^2 \rho\omega^2}{8E}x. \tag{B4}$$

Second harmonic 2 (4ω):

$$U_{h2} = \frac{\beta_2 U_1^2 \rho(2\omega)^2}{8E}x. \tag{B5}$$

Frequency-up conversion (3ω):

$$U_{\text{up}} = -\frac{\beta_2 U_0 U_1 \rho(\omega)(2\omega)}{4E}x. \tag{B6}$$

Frequency-down conversion (ω):

$$U_{\text{down}} = -\frac{\beta_2 U_0 U_1 \rho(\omega)(2\omega)}{4E}x. \tag{B7}$$

Herein, Eq. (B4) is a second harmonic generated by a fundamental wave, not secondary nonlinear phenomena so that has already been considered in Eq. (18). Also, considering that the amplitude of the second harmonic (U_1) is quite smaller than the fundamental wave (U_0), the effect of the Eq. (B5) is very small compared to other secondary nonlinear phenomena so it is negligible. Therefore, only the Eqs. (B6) and (B7), corresponding to frequency conversion, are considered secondary nonlinear phenomena whose amplitudes are sufficient to affect the harmonic tuning.

Analyzing the frequency conversion, Eqs. (B6) and (B7) both include the amplitude of the second harmonic (U_1). However, in reality, U_1 is not the boundary condition actuated from $x = 0$, but the amplitude of the second harmonic which is generated continuously as the wave propagates in a nonlinear medium. Therefore, the frequency conversion terms including U_1 should be recalculated. Considering the characteristics of nonlinear phenomena which are generated continuously according to the propagation distance of waves, Eqs. (B6) and (B7) can be rewritten as integral expressions as follows:

Frequency-up conversion (3ω):

$$U_{\text{up}} = \int_0^x -\frac{\beta_2 U_0 U_1 \rho(\omega)(2\omega)}{4E}dx. \tag{B8}$$

Frequency-down conversion (ω):

$$U_{\text{down}} = \int_0^x -\frac{\beta_2 U_0 U_1 \rho(\omega)(2\omega)}{4E}dx. \tag{B9}$$

As shown in Eq. (18), the amplitude of the second harmonic corresponding to U_1 is as follows:

$$U_1 = \frac{\beta_2 U_0^2 \rho\omega^2}{8E}x. \tag{B10}$$

Substituting Eq. (B10) into Eqs. (B8) and (B9), the amplitude of the frequency-up and -down conversion are obtained as follows:

Frequency-up conversion (3ω):

$$U_{\text{up}} = -\frac{\beta_2\rho}{4E}(U_0)\left(\frac{\beta_2 U_0^2 \rho\omega^2}{8E}\right)(\omega)(2\omega)\frac{x^2}{2}. \tag{B11}$$

Frequency-down conversion (ω):

$$U_{\text{down}} = -\frac{\beta_2\rho}{4E}(U_0)\left(\frac{\beta_2 U_0^2 \rho\omega^2}{8E}\right)(\omega)(2\omega)\frac{x^2}{2}. \tag{B12}$$
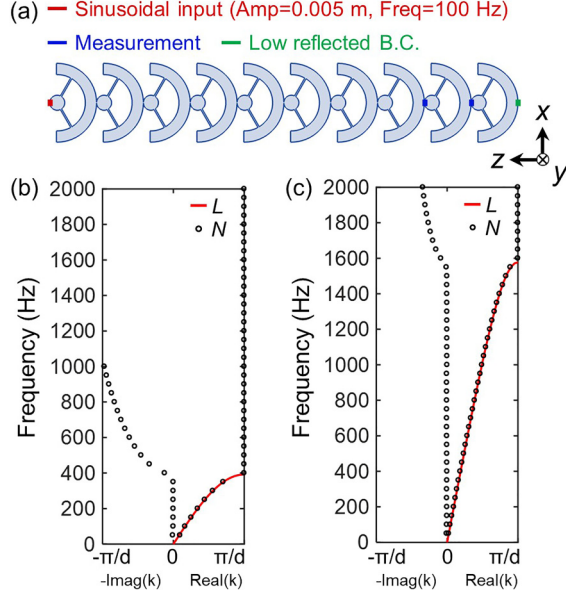
FIG. 13. (a) Numerical simulation settings to calculate wave dispersion curve for the nonlinear system, and plot of the wave dispersion curve calculated with the nonlinear simulation in (a) (black dots) and the general linear simulation (red line) for (b) $\theta = 0$ degrees, (c) $\theta = 30$ degrees.

Therefore, the frequency components generated by frequency conversion are expressed as follows:

frequency-up conversion (3ω):

$$u_{\text{up}}(x, t) = -\frac{\beta_2 \rho}{4E}(U_0)\left(\frac{\beta_2 U_0^2 \rho \omega^2}{8E}\right)(\omega)(2\omega)\frac{x^2}{2}$$
$$\times \cos 3(kx - \omega t). \quad \text{(B13)}$$

frequency-down conversion (ω):

$$u_{\text{down}}(x, t) = -\frac{\beta_2 \rho}{4E}(U_0)\left(\frac{\beta_2 U_0^2 \rho \omega^2}{8E}\right)(\omega)(2\omega)\frac{x^2}{2}$$
$$\times \cos (kx - \omega t). \quad \text{(B14)}$$

APPENDIX C: BAND STRUCTURE CONSIDERING GEOMETRIC NONLINEARITY

In the manuscript, the Floquet theory is adopted to calculate the band structure of the proposed metamaterials. However, since the Floquet theory is only valid in the linear case, there is an error if the Floquet theory is applied to the nonlinear system. Thus, it is essential to check whether the error is negligible or not. To this end, we newly carried out numerical nonlinear wave simulations to calculate the band structure for the nonlinear system. The detailed process is as follows: First, ten unit cells of the proposed metamaterial are arranged as shown in Fig. 13(a). Second, a displacement condition is imposed to the left end to actuate the longitudinal wave with the amplitude of 5 mm. Also, the low reflected boundary condition, consisting of a pseudo perfectly matched layer (pseudo-PML), is imposed to the right end to prevent reflected waves (more details about the pseudo-PML are described in Sec. III). Third, displacements are measured at the

eighth unit cell and the ninth unit cell of the metamaterial. Finally, the band structure is calculated by using the measured phase difference between the eighth unit cell and the ninth unit cell. Note that the simulation is a nonlinear simulation and thus the band structure is calculated for nonlinear system without using Floquet theory.

Figures 13(b) and 13(c) plot the band structure calculated by the aforementioned nonlinear simulation (in the black dots) and well-known linear simulation with the Floquet periodicity (in the red lines). As can be seen in Figs. 13(b) and 13(c), the calculated band structures are almost the same for both cases, indicating that the error occurred due to the Floquet theory is almost negligible. With this result, the use of the Floquet theory in the paper can be justified.

APPENDIX D: HIGHER ORDER HARMONICS OF THE FEASIBLE NONLINEARITY-TUNABLE METAMATERIAL

In the manuscript, we focused on nonlinear wave phenomena based on second- and third-order nonlinearities, but there also exist various higher harmonic waves due to the nonlinear nature. For instance, in the wave simulation in the manuscript with 100 Hz wave excitation, there are not only the waves with 200 and 300 Hz but also other waves such as the waves with 400 and 500 Hz. However, in the proposed metamaterials, the generation of 400 and 500 Hz waves is sometimes suppressed due to the bandgap of the metamaterial, as can be seen in Fig. 10, the proposed metamaterial may have a bandgap from 391.8 Hz so that both the 400 and 500 Hz waves are largely suppressed. In addition, the effect of higher-order nonlinear wave phenomena is relatively smaller than lower-order nonlinear wave phenomena at low frequencies and small amplitudes. In this study, since low frequency (100 Hz) and small amplitude (0.005 m) are used, the magnitude of the higher-order harmonics becomes much smaller than that of the second and third harmonics.

To clearly show the issues related to the higher harmonics, the numerical results with the transient simulation for harmonic generation in Fig. 12 is replotted to additionally cover higher frequency range. Figure 14 is the replotted frequency domain results. In Figs. 14(a)–14(c), the generation of 400 and 500 Hz waves are hard to see due to the bandgap effect or very small nonlinear effect. However, in Fig. 14(d), where the second-order nonlinear parameter has the maximum value, various peaks at 400 and 500 Hz are clearly seen, indicating that higher harmonics are generated. Nevertheless, the amount of the higher harmonics is not very large compared to the second and third harmonics.

As a result, we focused on the second and third harmonic waves in our simulation. Note that it is same in practical applications such as the directional acoustic speaker or nonlinear NDE; only the second or third harmonic waves are mainly considered while there exist other higher harmonics.

APPENDIX E: FORWARD AND BACKWARD EXCITATION

Since the unit cell has asymmetric configuration along the wave propagation direction, the unit cell would have the well-known Willis coupling and nonreciprocity could be found. To check the possible nonreciprocity, the transmittance and
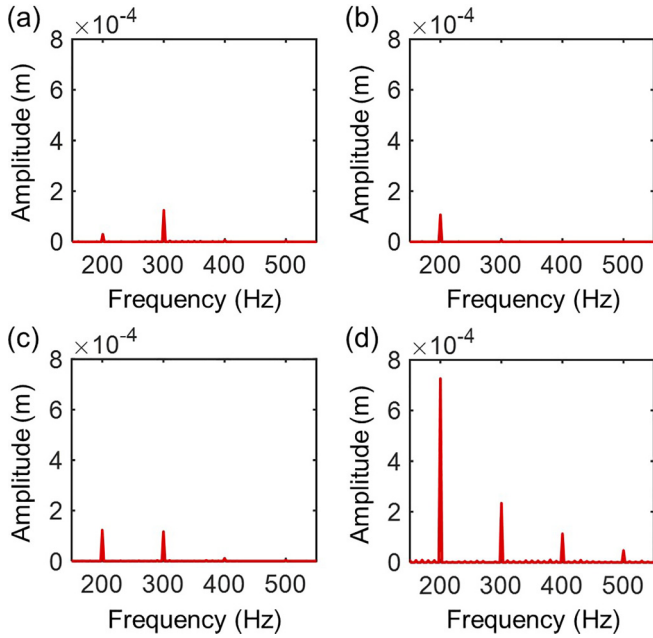
FIG. 14. Frequency domain data for harmonics up to fifth order with the initial angle of (a) 0 degrees, (b) 26.57 degrees, (c) 0.5 degrees, (d) 7 degrees.

reflectance of the metamaterial is measured for forward and backward excitation. The corresponding simulation setup is shown in Fig. 15(a). As shown in Fig. 15(a), ten unit cells of the proposed metamaterial are arranged. On both sides of the metamaterial, two plates, each with the same thickness and material as the metamaterial, are placed. The PML is imposed to the ends of the two plates to prevent reflected waves. For forward and backward excitation, the longitudinal wave is actuated with the amplitude of 0.005 m and 100 Hz at the interface between the plate and the PML. To measure transmitted and reflected waves, displacements are measured at four points on both plates. Note that the main goal of the simulation is to check the possible nonreciprocal behavior, so nonlinear effects were not considered at all.

The numerical results in Figs. 15(b)–15(e) show the amplitudes and phases of both transmitted and reflected waves.
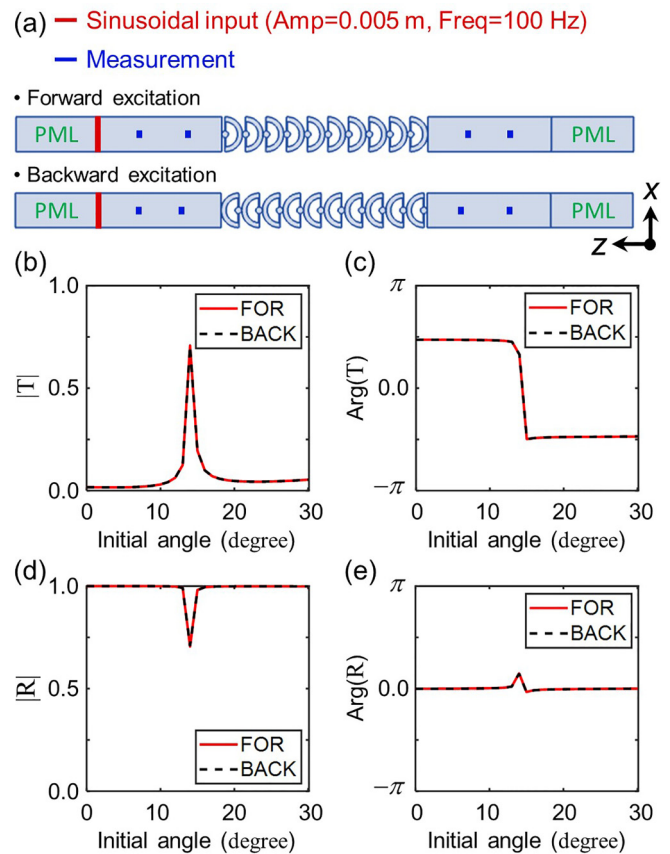

FIG. 15. (a) Numerical simulation settings to check the nonreciprocity. Numerical results for forward and backward excitation of (b) amplitudes and (c) phases of transmitted wave, (d) amplitudes and (e) phases of reflected wave, respectively.

Figures 15(b) and 15(d) demonstrate that the amplitudes of transmittance and reflectance are the same for both forward and backward excitation, which is obvious since the system is a linear system. In addition, Figs 15(c) and 15(e) show that the phase shifts are also same for both forward and backward excitation, indicating that the Willis coupling is almost negligible.

[1] S. Yao, X. Zhou, and G. Hu, New J. Phys. **10**, 043020 (2008).

[2] J. Li and C. Chan, Phys. Rev. E **70**, 055602(R) (2004).

[3] Y. Ding, Z. Liu, C. Qiu and J. Shi., Phys. Rev. Lett. **99**, 093904 (2007).

[4] X. N. Liu, G. K. Hu, G. L. Huang, and C. T. Sun, Appl. Phys. Lett. **98**, 251907 (2011).

[5] Y. Wu, Y. Lai, and Z. Q. Zhang, Phys. Rev. Lett. **107**, 105506 (2011).

[6] X. Zhou, X. Liu, and G. Hu, Theor. Appl. Mech. Lett. **2**, 041001 (2012).

[7] J. H. Oh, Y. E. Kwon, H. J. Lee, and Y. Y. Kim, Sci. Rep. **6**, 23630 (2016).

[8] J. H. Oh, H. M. Seung, and Y. Y. Kim, Appl. Phys. Lett. **108**, 093501 (2016).

[9] Y. Chen, G. Hu, and G. Huang, J. Mech. Phys. Solids **105**, 179 (2017).

[10] T. A. Hewage, K. L. Alderson, A. Alderson, and F. Scarpa, Adv. Mater. **28**, 10323 (2016).

[11] S. Babaee, J. Shim, J. C. Weaver, E. R. Chen, N. Patel, and K. Bertoldi, Adv. Mater. **25**, 5044 (2013).

[12] K. Bertoldi, V. Vitelli, J. Christensen, and M. Van Hecke, Nat. Rev. Mater. **2**, 1 (2017).

[13] H. Wang, Y. Zhang, W. Lin, and Q. H. Qin, Comput. Mater. Sci. **171**, 109232 (2020).

[14] J. H. Oh and B. Assouar, Sci. Rep. **6**, 33410 (2016).

[15] H. W. Park, H. M. Seung, M. Kim, W. Choi, and J. H. Oh, Phys. Rev. Appl. **15**, 024008 (2021).

[16] V. E. Gusev and O. B. Wright, New J. Phys. **16**, 123053 (2014).

[17] R. Zhu, X. Liu, G. Hu, C. Sun, and G. Huang, Nat. Commun. **5**, 5510 (2014).

[18] H. W. Park and J. H. Oh, Sci. Rep. **9**, 13973 (2019).

[19] X. Zhou and G. Hu, Appl. Phys. Lett. **98**, 263510 (2011).

[20] H. Lee, J. H. Oh, H. M. Seung, S. H. Cho, and Y. Y. Kim, Sci. Rep. **6**, 24026 (2016).

[21] G. J. Jeon and J. H. Oh, Phys. Rev. E **103**, 012212 (2021).

[22] R. Khajehtourian and M. I. Hussein, AIP Adv. **4**, 124308 (2014).

[23] M. H. Bae and J. H. Oh, J. Mech. Phys. Solids **139**, 103930 (2020).

[24] M. H. Bae and J. H. Oh, Mech. Syst. Signal Process. **170**, 108832 (2022).

[25] C. Chong, M. A. Porter, P. G. Kevrekidis, and C. Daraio, J. Phys.: Condens. Matter **29**, 413003 (2017).

[26] A. Amendola, A. Krushynska, C. Daraio, N. M. Pugno, and F. Fraternali, Int. J. Solids Struct. **155**, 47 (2018).

[27] M. Miniaci, M. Mazzotti, A. Amendola, and F. Fraternali, Int. J. Solids Struct. **216**, 156 (2021).

[28] M. F. Berwind, A. Kamas, and C. Eberl, Adv. Eng. Mater. **20**, 1800771 (2018).

[29] J. Hua, H. Lei, C. F. Gao, X. Guo, and D. Fang, Extreme Mech. Lett. **35**, 100640 (2020).

[30] T. Chen, M. Pauly, and P. M. Reis, Nature (London) **589**, 386 (2021).

[31] G. J. Simitses, *An Introduction to Elastic Stability of Structures* (Prentice-Hall, Englewood Cliffs, NJ, 1976).

[32] E. T. Enikov, S. S. Kedar, and K. V. Lazarov, J. Microelectromech. Syst. **14**, 788 (2005).

[33] J. J. Rushchitsky, *Nonlinear Elastic Waves in Materials* (Springer International Publishing, Heidelberg, 2014), p. 164.

[34] W. T. Yost and J. H. Cantrell, in *IEEE 1992 Ultrasonics Symposium Proceedings, Tucson, AZ, USA*, Vol. 2 (1992), pp. 947–955.